Photothermal circular dichroism studies of single nanoparticles

Späth, P.R.

5

Magnetic circular dichroism of superparamagnetic nanoparticles

Magnetic imaging is a versatile tool in biological and condensed-matter physics. Existing magnetic imaging techniques either require demanding experimental conditions which restrict the range of their applications or lack the spatial resolution required for single-particle measurements. Here, we combine photothermal (PT) microscopy with magnetic circular dichroism (MCD) to develop a versatile magnetic imaging technique using visible light. Unlike most magnetic imaging techniques, photothermal magnetic circular dichroism (PT MCD) microscopy works particularly well for single nanoparticles immersed in liquids. As a proof of principle, we demonstrate magnetic CD imaging of superparamagnetic magnetite nanoparticles immersed in microscope immersion oil. The sensitivity of our method allowed us to probe the magnetization curve of single $\sim$*400* nm*-diameter magnetite nanoparticles.*

5.1. Introduction

Light-matter interaction in magnetic materials gives rise to unique magneto-optical phenomena like the Faraday and Kerr effects. Ultrafast spectroscopy with femtosecond pulsed lasers enables manipulation of magnetic properties such as magnetization reversal [1] or demagnetization of ferromagnetic metallic thin films [2]. Magnetic nanoparticles are promising candidates for applications in biomedicine, spintronics and data storage [3, 4]. Magnetite (Fe_3O_4) nanoparticles, because of their size-dependent magnetic properties and biocompatibility, have been used for bioimaging, for photothermal [5] and magnetothermal cancer treatment [6]. For magnetic data storage, the minimum size of a magnetic bit is limited by the so-called *superparamagnetic limit* [7, 8]. Superparamagnetism occurs in ferromagnetic and ferrimagnetic materials. Bulk magnetite shows ferrimagnetic behaviour. Single-domain magnetite nanoparticles of sufficiently small size randomly flip their magnetization direction, on the timescale of laboratory experiments (s-hrs), when the magnetic energy barrier is on the order of, or smaller than the thermal energy [9]. When the measurement time is longer than the average time between two magnetization flips, the particle appears to carry no average magnetic moment. Just as paramagnetic particles, superparamagnetic ones can be magnetized under an external magnetic field, but typically exhibit much larger susceptibility. To study magnetic phenomena of single nanoparticles one can use non-optical devices such as SQUIDs (superconducting quantum interference devices) and MFMs (magnetic force-microscopes), or X-ray beam techniques such as XMCD (X-ray magnetic circular dichroism). Conventional SQUID magnetometers detect the net signal from large ensembles of nanoparticles, averaging out the size-dependent magnetic properties of the nanoparticles. For imaging purposes, scanning-SQUID microscopy can be used to image the magnetic flux from individual particles - in some cases with sub-$100\,\mathrm{nm}$ resolution [10]. Owing to their exceptional sensitivity, down to individual single-molecule magnets [11], SQUIDs are therefore widely used in the study of magnetic nanostructures [12], however, they require a cryogenic environment, complex probes and electronics, which can be difficult to implement for many applications. MFM is a considerably simpler technique with excellent spatial resolution and can operate at ambient conditions. However, MFM also faces drawbacks such as topographic cross talk and the magnetic distortions caused by the strong stray fields of the probe [13]. Furthermore, when studying samples in external magnetic fields, not only the sample but also the probing tip is influenced by the field [14]. XMCD provides high spatial resolution and sensitivity in the study of single nanoparticles [15], but it requires access to a beam line.

Magnetic circular dichroism (MCD) spectroscopy [16, 17] is an optical technique that exploits the polar Kerr effect [18]. Until now conventional visible-light MCD spectroscopy has only been used to investigate magnetic nanoparticles [16] or (bio-) molecules [17] in solutions containing an ensemble of many nanoparticles. The investigation of size- and shape-dependent magnetic properties, however, demands single-particle resolution. XMCD and electron holography measurements of single particles show that the magnetic properties not only depend on their size, but also on their shape, and on temperature [15, 19]. For instance, cobalt and iron particles in the range of $8\,\mathrm{nm}$ to $20\,\mathrm{nm}$ can exhibit both ferromagnetic and superparamagnetic behaviors at room temperature [20]. Distinctions in magnetic behaviour due to shape and size cannot be made by measuring an ensemble of nanoparti-

cles, and yet, they are of vital importance to their applications in biomedical sciences and spintronic devices. Here, we overcome the limitation of visible-light MCD to ensemble measurements by implementing our newly developed Photothermal circular dichroism (PT CD) microscopy [21, 22] for magnetic imaging of single nanoparticles. To image the magnetization of nanoparticles, PT MCD is considerably simpler as, for example, XMCD or scanning SQUID, making it far more accessible. Our method directly measures the absorption of individual particles via their PT response. As the absorption linearly scales with the particle's volume we can access the particle's size. The MCD signal, which we can determine separately via PT MCD measurements, displays a linear dependence on the particle's magnetization [18, 23]. Our measurements therefore allow us to simultaneously access the size and the magnetization of individual particles.

Figure 5.1 shows a scheme of our PT MCD setup. The setup is a photothermal microscope [24] augmented with polarization modulation optics in the heating arm to facilitate photothermal circular dichroism measurements [21]. We use a dual modulation of the polarization because it offers excellent rejection of cross talk between linear and circular dichroism as discussed in chapter 3. By modulating either the intensity or the polarization of the heating beam, we can access absorption signals such as the total absorption (PT) as well as LD (linear dichroism) and CD. We use a Koehler configuration for the heating beam illumination but we strongly focus the probe beam. Thereby, the optical resolution at the probing wavelength ($780\,\mathrm{nm}$) remains diffraction-limited while the polarization state of the heating light ($532\,\mathrm{nm}$) remains well preserved. In circular dichroism mode our technique measures the differential absorption between left- and right-circularly polarized light and therefore is most sensitive to magnetic moments that are parallel (or anti parallel) to the propagation direction of the light. To measure PT CD in the presence of an external magnetic field (PT MCD), a long cylindrical permanent magnet (NdFeB, $3\,\mathrm{mm}$ diameter, $10\,\mathrm{cm}$ length) is used to provide an out-of-plane magnetic field at the sample such that the light propagation is parallel to the magnetization direction (optical z-axis). The magnetic field strength and sign can be varied by altering the distance and by flipping the orientation of the magnet relative to the sample.

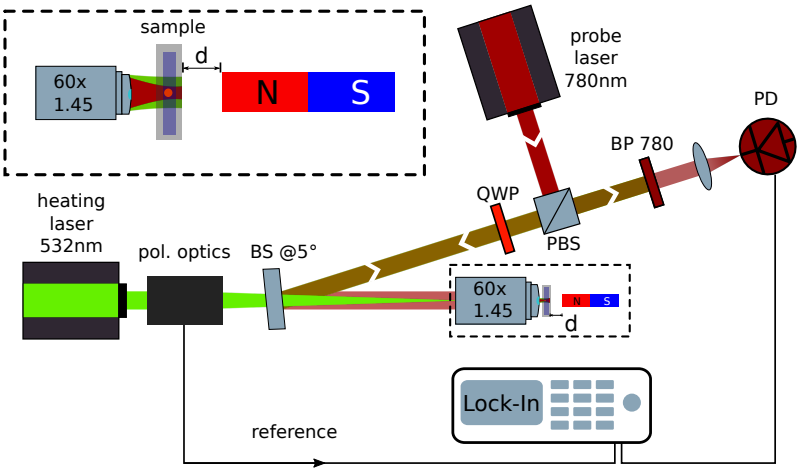

Figure 5.1: Schematic setup of the photothermal circular dichroism microscope. The $532\,\mathrm{nm}$ continuous wave (CW) heating laser beam is passed through a combination of polarization optics which modulates the polarization of the light between left- and right- circularly polarized at $\sim 100\,\mathrm{kHz}$. The $780\,\mathrm{nm}$ CW probe laser is passed through a combination of a polarizing beam-splitter (PBS) and a quarter-wave plate (QWP) and combined with the heating beam at the 50/50 beam-splitter (BS) at an angle of about $5°$. The sample is illuminated with the heating beam in a Koehler configuration, whereas the probe beam is focused at the sample through an oil-immersion objective (NA = 1.45). The collected probe light is filtered from the heating light with a band-pass filter (BP 780). The photothermal signal is isolated by a lock-in amplifier. A long cylindrical permanent magnet is placed perpendicular to the sample plane at a variable distance d to apply a magnetic field to the sample. The inset shows an enlarged view of the heating and probe beam illumination and the position of the magnet relative to the sample. To flip the magnetic field direction, the magnet's poles are flipped. A polarization optics unit consists of two polarization modulators, driven at two different frequencies ω_1 and ω_2. An additional set of static birefringent plates and a polarizer enable polarization and amplitude modulation of the heating beam as described in chapter 3. A reference signal at the sum frequency ω_1+ω_2 of the two modulators is sent to the lock-in amplifier.

5.2. Results and discussion

Here we study nominally $200\,\mathrm{nm}$-diameter magnetite nanoparticles (Chemicell GmbH) in a variable magnetic field. The tunable magnetic field enables us to discern MCD from geometric CD. Geometric CD is induced by the chiral structure of an object [25]. In contrast to geometric CD, MCD in ferro- and ferrimagnetic materials results from the polar magneto-optic Kerr effect [18, 23]. The Kerr effect is induced by magnetic perturbations of the electronic states involved in optical transitions. It results from the interaction between electrons that provide magnetic moments and those that have large spin-orbit coupling [18, 26].

A single-crystalline magnetite particle of $200\,\mathrm{nm}$-diameter is expected to have multiple magnetic domains and, moreover, it will exhibit magnetic remanence. The particles used

here, however, are clusters of sub-15-nm single crystals. At room temperature, magnetite particles of such size show superparamagnetic behavior. When they form clusters in a wet chemical process they can maintain their superparamagnetic behaviour due to weak magnetic coupling between the individual subunits [19, 27, 28].

To show that PT MCD can indeed provide images of single nanoparticles with magnetic contrast and to discern magnetic effects from shape effects (geometric chirality) we spin-coated the nominally $200\,\mathrm{nm}$-diameter magnetite particles on a glass surface at very low surface coverage ($\sim$1 NP/10 $\mu\mathrm{m}^2$). We then obtain a series of four images as displayed on a selected example in figure 5.2 (a-d):

(a) A photothermal image, which allows us to estimate the particles' volume due to the linear relationship between absorption cross section and volume. (b) A photothermal CD image in the absence of an external magnetic field, which allows us to determine the geometric CD of individual particles. (c) and (d) PT CD images obtained with axial magnetic fields of positive (c) and negative sign (d). The axial magnetic field gives rise to a polar Kerr effect which can be detected by our setup via PT MCD.

The PT scan (figure 5.2 a) indicates a broad size distribution of the particles. Based on the correlated SEM images, (see figure S5.1) we estimate the size of the three bright particles to be about $400\,\mathrm{nm}$. Upon application of an external magnetic field we find a strong contrast in the CD images (figure 5.2 (c-d)), indicating the presence of a net magnetic moment in the particles, which generates a strong MCD signal. We find that all particles exhibit the same sign of CD and that, upon inversion of the magnetic field, we invert the sign of the CD signal, corroborating the MCD nature of the signal. We then compare the relative magnetic susceptibility of the individual magnetite particles by calculating their g-factor, which is defined as

$$g = 2 \cdot \frac{A_{lcp} - A_{rcp}}{A_{lcp} + A_{rcp}}, \tag{5.1}$$

where A_{lcp} and A_{rcp} are the absorptivities for left- and right-handed circular polarized light, respectively. We can simply retrieve the g-factor by calculating the ratio of CD over PT signals. The MCD signal is proportional to the magnetic moment while the PT signal is proportional to the volume of the particle and thus to its number of unit cells. By taking their ratio we obtain a value that scales with the magnetic moments per unit cell. We find that all particles have similar g-factors, close to 1% at a magnetic field of $0.4\,\mathrm{T}$, indicating a similar magnetic susceptibility. Figure 5.2(b) shows a CD scan in the absence of a magnetic field. We find that even in the absence of a magnetic field some particles exhibit CD. We assign this offset CD to geometric chirality that can occur in quasi-spherical particles [21, 29] and is different from particle to particle (see figure S5.5 and S5.6).

Thanks to the excellent SNR of the measurements in figure 5.2, we are not limited to measurements of the MCD close to the saturation magnetization of the magnetite particles. This motivated us to obtain the magnetization curve of a single $\sim$400 nm magnetite particle. We did this by focusing on a single $400\,\mathrm{nm}$-diameter particle and measuring its MCD signal while the magnetic field's strength and sign were varied by altering the magnet's distance to the sample and flipping its orientation. In order to obtain the magnetic field strength as a function of distance we performed a calibration measurement (see figure S5.4) using a Gaussmeter (Hirst Magnetic Instruments GM08). The resulting magnetisation curve of

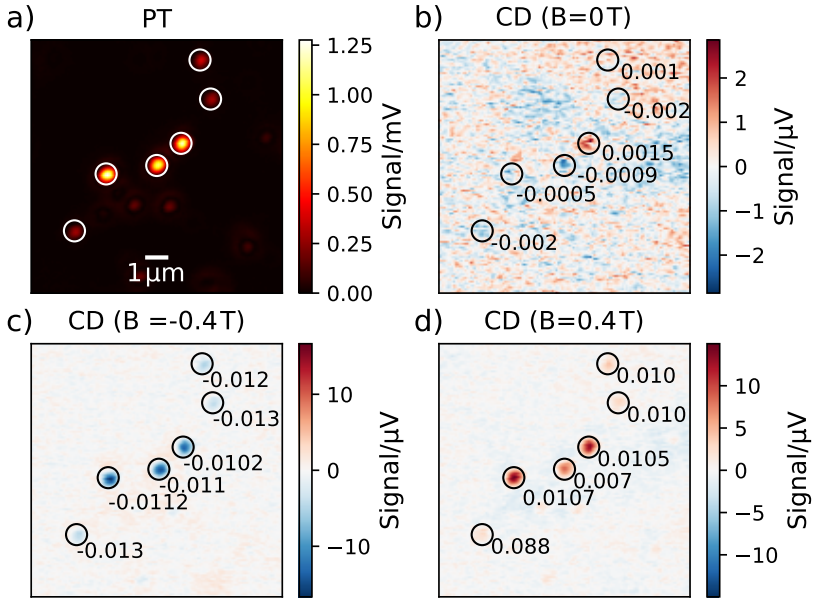

Figure 5.2: Photothermal (a) and circular dichroism measurements (b-d) of nominally 200 nm-diameter magnetite particles exposed to different external magnetic fields. The actual size of the three brighter particles in the center is measured by correlative SEM imaging and falls into the range of 300-400 nm (see figure S5.1 and S5.2). For details about the sizing see figure S5.1-S5.2. The integration time is 20 ms per pixel. The magnetic field strength for b), c) and d) is 0 T, −0.4 T and 0.4 T, respectively. Individual particles exhibiting considerable MCD are marked with circles and numbers indicate their g-factors. At an external field of 0.4 T the g-factors are close to 1% for most particles.

a single magnetite particle is displayed in figure 5.3. The shape of the curve displays superparamagnetic behaviour, as evident from the absence of a remanent magnetization. The field we apply here (∼0.43 T) is larger than the saturation field of our nanoparticles (subunit size of 8-13 nm) [31] and below the saturation field of bulk magnetite [32]. To exclude possible effects of the external magnetic field on the optical elements that may induce an artificial CD, we performed a reference measurement on a 100 nm-diameter gold nanoparticle (see orange data points in figure 5.3). Gold is diamagnetic and therefore has a very small magnetic susceptibility [33]. The small susceptibility should result in a negligible MCD response, compared to magnetite. If the CD signal of the magnetic particles was due to the external magnetic field affecting the setup (i.e. the objective) we would also expect a response of the gold nanoparticles upon application of an external magnetic field. The shape of the gold nanoparticle's PT CD curve shows that this particle had no significant response to the external magnetic field, within experimental noise. Together, these observations provide strong evidence that the observed strong MCD response of our magnetite particles is

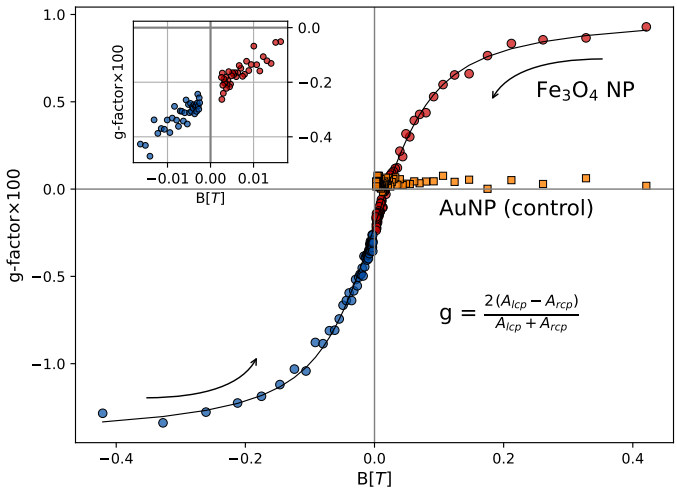

Figure 5.3: Magnetization curve of a single $\sim$400 nm-diameter magnetite particle measured by PT CD in hexadecane. The shape displays superparamagnetic behaviour. The integration time is 1 s per point. The inset shows a magnified view of the magnetite nanoparticle's magnetization curve at small fields. Arrows indicate the sweep direction of the magnetic field (strong-to-weak). The orange data points show a reference measurement on a 100 nm-diameter gold nanoparticle, here only for positive magnetic fields. The solid line is a fit with a Langevin function: ($\coth(x)$-1/x, where x = μ_B/k_BT) [30]. The resulting magnetic moment of the composing nanoparticles is about 10,000 Bohr magnetons.

indeed induced by their magnetic moment. The shape of the curve and the saturation magnetization that we find are in reasonable agreement with ensemble measurements for other magnetite nanoparticles [34], however, the strength of the MCD effect (g-factor) that we observe is one order of magnitude larger than found elsewhere in ensemble measurements [35, 36]. One reason for the difference in g-factor could be a different subunit size of the particles used in these studies which were between 3.4 and 6.9 nm, compared to 8-13 nm for our particles. Nanocrystals of smaller size exhibit a smaller saturation magnetization due to a magnetic dead layer [31]. Another possible reason for the difference could be the different measurement modality. While refs [35, 36] measure in a transmission geometry thereby probing extinction we employ PT contrast, probing absorption. Extinction measurements and absorption are not in general equivalent as the extinction measurement also entails a considerable scattering contribution.

5.3. Conclusion and outlook

We have demonstrated a PT-based optical imaging method that enables the study of single-particle magnetization via PT MCD. The excellent sensitivity of PT imaging allowed us to obtain single-particle magnetization curves. Our single-particle and absorption based measurements revealed g-factors that are one order of magnitude higher than the ones found

by ensemble extinction-based studies [35, 36]. The images presented in figure 5.2 were obtained by scanning the sample with a piezo-stage and thus require long image acquisition times. Recent advances in the field of wide-field PT imaging [37–39], that use cameras instead of confocal scanning, could open the possibility for faster image acquisition with magnetic contrast. PT imaging is particularly well suited for studying the absorption of small particles, since the absorption scales with the volume. From our signal-to-noise ratios and the available laser powers of probe and heating lasers we estimate that the magnetic moments of single-domain magnetite particles with sizes down to $20\,\mathrm{nm}$ can be studied with our technique. We believe that photothermal magnetic circular dichroism (PT MCD) is a promising technique for future studies of magnetic nanoparticles as it is easy to implement in existing PT setups and does not suffer from the drawbacks of complex instrumentation and restrictive demands on experimental environments imposed by other methods like XMCD, MFM or scanning SQUIDs.

5.4. Supplementary information

5.4.1. Correlated SEM images of nominally 200 nm particles.

Figure S5.1 shows a SEM image of the same area as the images of figure 5.2. The sample surface is partially sullied with glass debris that probably came during the manufacturing process of markers on the glass slide (ibidi Gridded Glass Coverslips). The diameter of the encircled particles is significantly larger than $200\,\mathrm{nm}$. However, the SEM scan, which was performed under 30° of the sample, also reveals that the particles are not spherical in shape. In fact they are rather flat. The three marked particles on the top right, for example, have the similar strength in PT signal and therefore should have the same volume. From the SEM images the particle looks smaller in diameter than the lower ones but appears significantly higher. From the tilted SEM images and the estimated height we estimate the volume of the particles to be equivalent to a sphere of $\sim 400\,\mathrm{nm}$ in diameter.

5.4.2. PT of 20 nm magnetite particles

Due to the small tilt of the SEM scans in figure S5.1 (30°) and the crude shape of the particles we wanted to recheck the particle's size by comparing their absorption with well characterized $20\,\mathrm{nm}$-diameter (Nanocomposix) magnetite particles. Based on the PT signal of the $20\,\mathrm{nm}$-diameter magnetite particles, assuming that the absorption scales linearly with the volume, we can extrapolate the size of the supposedly $200\,\mathrm{nm}$ particles. The PT scans of three areas of a sample of spin-coated $20\,\mathrm{nm}$-diameter magnetite particles are shown in figure S5.2. Note the presence of a weak background PT signal that probably occurs due to weak absorption in the glass slide. This is only visible due to the weak absorption of the magnetite nanoparticles and the relatively large heating power ($\sim 60\,\mathrm{mW/\mu m^2}$). Figure S5.3 (c) shows a histogram of the PT signals of 193 magnetite nanoparticles and (d) a TEM micrograph, provided by the manufacturer. The absorption scales linearly with the particle's volume. Accordingly the histogram of the cubic root of PT signals scales linearly with the particle size. Figure S5.3 (a) and (b) show the histogram of the cubic root of PT signals and the histogram of diameters measured by the manufacturer via TEM, respectively. The

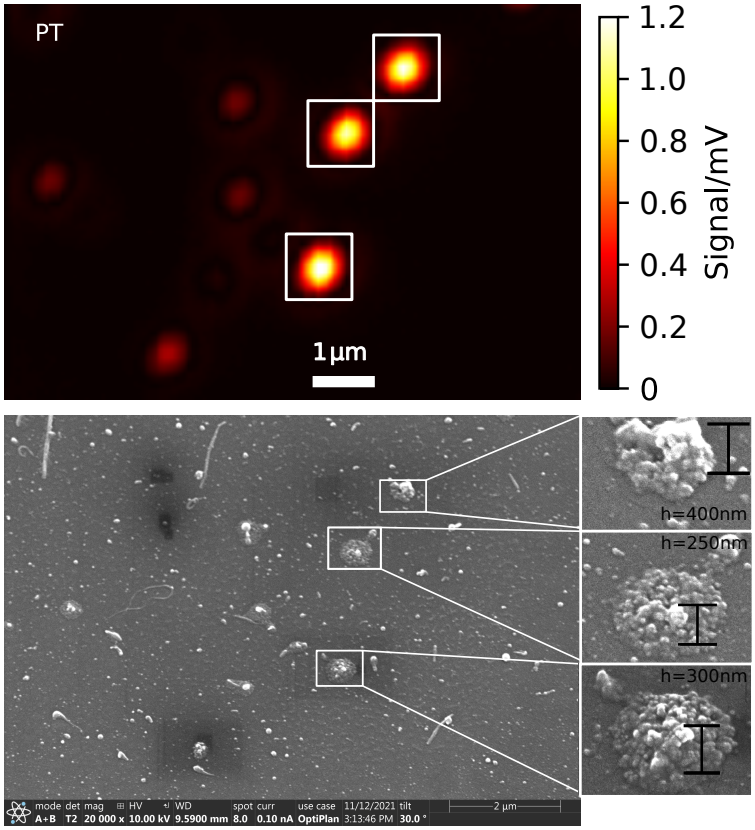

Figure S5.1: Correlated SEM images of the scanned area in figure 5.2. The top panel shows the PT image of the same sample region, which was rotated and mirrored compared to figure 5.2 to fit with the SEM micrograph in the lower panel. The square boxes are guides for the eye. The particles diameter is much larger than the 200 nm given by the manufacturer, however, the tilted SEM scan (30°) indicates that the particles are rather flat. The black bar indicates the estimated heights of the particles.

shape of the histogram of particle sizes based on the PT measurements agrees well with the histogram based on the manufacturer's TEM measurements (c,d). We can therefore assume that the center of the histogram in (a) corresponds to the center of the histogram in (b).

Based on the ratio of optical powers ($\times$48) and the ratio of the respective PT signals ($\times$1/52) we estimate the size of the supposedly 200 nm particles to be $\sim$300 nm. We therefore believe that the size of 400 nm that we found by SEM imaging is reasonable.

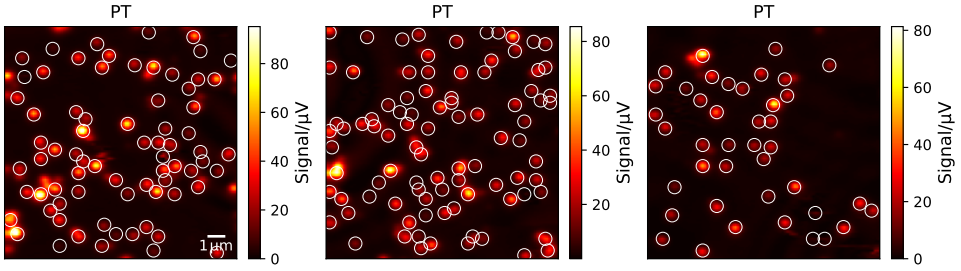

Figure S5.2: PT scans of 193 20 nm-diameter particles from 3 different areas on the sample. The white circles are guides for the eye.

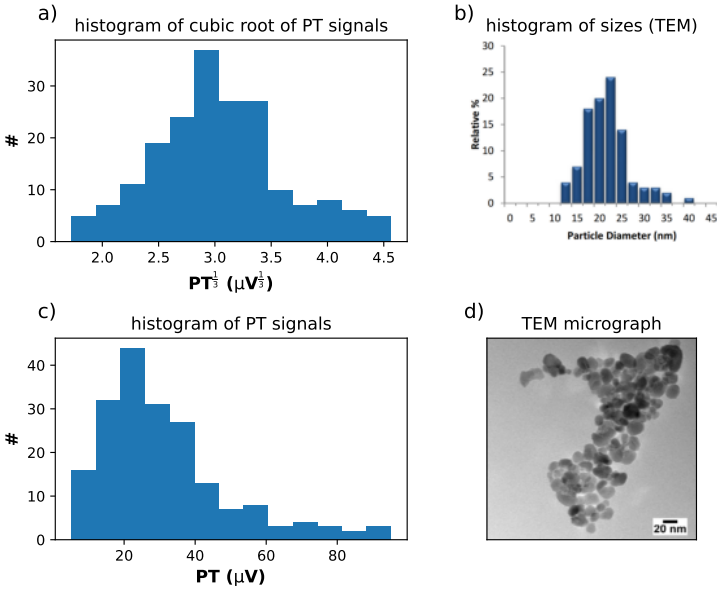

Figure S5.3: (a) and (c) histogram of PT signals of 193 20 nm-diameter nanoparticles. b) size histogram from the manufacturer (NanoComposix) based on TEM imaging from the same particle batch. (d) TEM micrograph of the particles.

5.4.3. Calibration of magnetic field vs distance

Figure S5.4 shows the magnetic field dependence on distance of the permanent magnet we used to vary the magnetic field, measured with a Gaussmeter (Hirst Magnetic Instruments GM08) and the fitted data that is used to interpolate the field values at the positions relevant for the measurements of figure 5.3. We fit the data with the following phenomenological

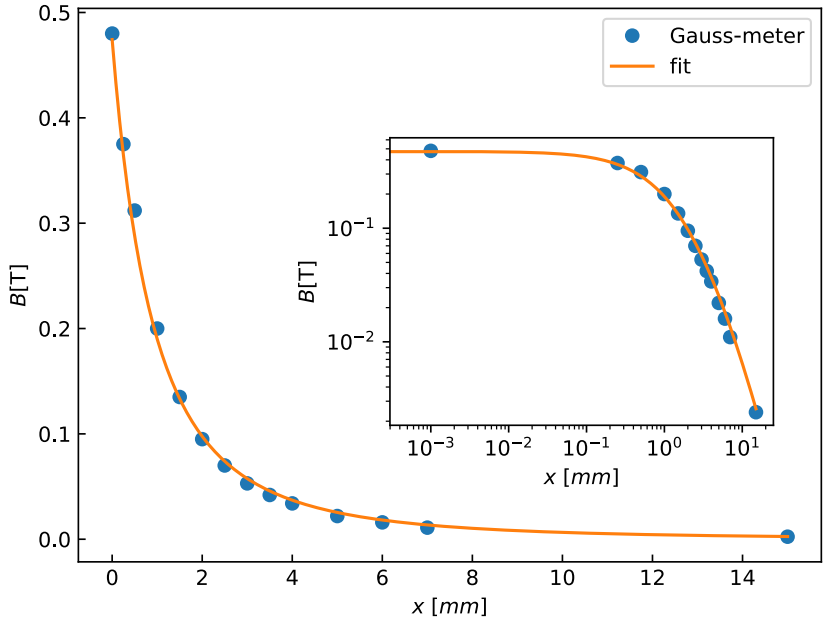

Figure S5.4: Measured dependence of magnetic field on distance (blue) and a phenomenological fit (orange). The magnetic field was measured wit a Gaussmeter. The insert shows a double logarithmic plot of the measured and fitted field dependence on distance.

function:

$$B(x) = \frac{a}{(x+b)^2} \cdot \frac{1}{(1+x/c)} \tag{5.2}$$

For small distances we assume a a/(x+b)^2 dependence of the field, since the magnet is very long (monopole limit) with respect to its diameter. To improve the fit for larger distances where dipole effects come into play, we multiply by a factor of 1/(1+x/c). The respective values of a,b and c are: $1.85\,\mathrm{T{\cdot}mm^2}$,$1.97\,\mathrm{mm}$ and $10.04\,\mathrm{mm}$.

5.4.4. Magnetic-field-dependent PT-CD curves

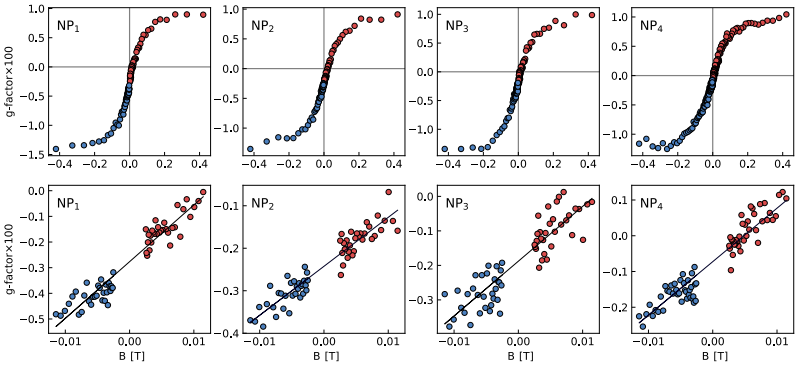

Figure S5.5: Magnetic-field-dependent circular dichroism curves of four different magnetite particles of $\sim$400 nm in diameter. The lower row shows a magnified view of the magnetization curve at smaller magnetic fields with a linear fit.

Figure S5.5 shows the magnetic field dependent PT-CD curves of four magnetite particles (NP1-NP4). All particles show similar g-factors indicating similar magnetic susceptibility. We can observe that the two parts of the magnetization curve (red and blue) seem to meet at zero magnetic field, within noise. This indicates the absence of a remanence magnetization. The offset values all have the same sign. This might give rise to the assumption of a bias in the the CD measurements, due to the particles themselves or due to the method. We have shown in chapter 3 that our optical method is not subject to artificial bias signals. To rule out biasing effects of the particles we used the same sample as for the magnetization-curve measurements, and performed a MCD scan including many particles.

Figure S5.6 (a) shows a PT and three CD images with (b) zero, (c) positive and (d) negative magnetic fields applied. When the magnetic field is turned off (figure S5.6 (b)) we still observe some residual CD signal that we relate to geometric chirality. We observe both positive and negative CD signals at zero external field. We therefore conclude that the four negative offset signals in figure S5.5 are not systematic.

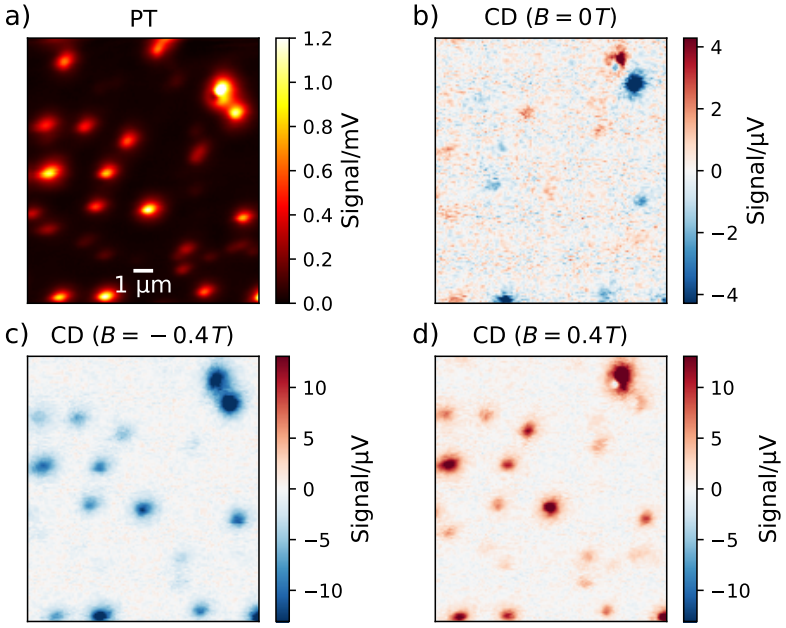

Figure S5.6: Photothermal (a) and photothermal CD images (b-d) a of nominally 200 nm superparamagnetic magnetite particles at different external magnetic fields.

References

[1] Stanciu, C.; Hansteen, F.; Kimel, A.; Kirilyuk, A.; Tsukamoto, A.; Itoh, A.; Rasing, T. All-Optical Magnetic Recording With Circularly Polarized Light. *Physical Review Letters* **2007**, *99*, 047601.

[2] Bigot, J.-Y.; Vomir, M.; Beaurepaire, E. Coherent Ultrafast Magnetism Induced by Femtosecond Laser Pulses. *Nature Physics* **2009**, *5*, 515–520.

[3] Mahmoudi, M.; Sant, S.; Wang, B.; Laurent, S.; Sen, T. Superparamagnetic Iron Oxide Nanoparticles (SPIONs): Development, Surface Modification and Applications in Chemotherapy. *Advanced Drug Delivery Reviews* **2011**, *63*, 24–46.

[4] Reiss, G.; Hütten, A. Magnetic Nanoparticles: Applications Beyond Data Storage. *Nature Materials* **2005**, *4*, 725–726.

[5] Shen, S.; Wang, S.; Zheng, R.; Zhu, X.; Jiang, X.; Fu, D.; Yang, W. Magnetic Nanoparticle Clusters for Photothermal Therapy With Near-Infrared Irradiation. *Biomaterials* **2015**, *39*, 67–74.

[6] Kobayashi, T. Cancer hyperthermia using magnetic nanoparticles. *Biotechnology journal* **2011**, *6*, 1342–1347.

[7] Skumryev, V.; Stoyanov, S.; Zhang, Y.; Hadjipanayis, G.; Givord, D.; Nogués, J. Beating the Superparamagnetic Limit With Exchange Bias. *Nature* **2003**, *423*, 850–853.

[8] Weller, D.; Moser, A. Thermal Effect Limits in Ultrahigh-Density Magnetic Recording. *IEEE Transactions on Magnetics* **1999**, *35*, 4423–4439.

[9] Néel, L. Théorie du traînage magnétique des ferromagnétiques en grains fins avec applications aux terres cuites. *Ann. Géophys.* **1949**, *5*, 99–136.

[10] Vasyukov, D.; Anahory, Y.; Embon, L.; Halbertal, D.; Cuppens, J.; Neeman, L.; Finkler, A.; Segev, Y.; Myasoedov, Y.; Rappaport, M. L., et al. A Scanning Superconducting Quantum Interference Device With Single Electron Spin Sensitivity. *Nature Nanotechnology* **2013**, *8*, 639–644.

[11] Wernsdorfer, W.; Sessoli, R. Quantum phase interference and parity effects in magnetic molecular clusters. *Science* **1999**, *284*, 133–135.

[12] Buchner, M.; Höfler, K.; Henne, B.; Ney, V.; Ney, A. Tutorial: Basic Principles, Limits of Detection, and Pitfalls of Highly Sensitive SQUID Magnetometry for Nanomagnetism and Spintronics. *Journal of Applied Physics* **2018**, *124*, 161101.

[13] Kazakova, O.; Puttock, R.; Barton, C.; Corte-León, H.; Jaafar, M.; Neu, V.; Asenjo, A. Frontiers of Magnetic Force Microscopy. *Journal of Applied Physics* **2019**, *125*, 060901.

[14] Weis, T.; Krug, I.; Engel, D.; Ehresmann, A.; Hoeink, V.; Schmalhorst, J.; Reiss, G. Characterization of Magnetic Force Microscopy Probe Tip Remagnetization for Measurements in External In-Plane Magnetic Fields. *Journal of Applied Physics* **2008**, *104*, 123503.

[15] Balan, A.; Derlet, P. M.; Rodríguez, A. F.; Bansmann, J.; Yanes, R.; Nowak, U.; Kleibert, A.; Nolting, F. Direct Observation of Magnetic Metastability in Individual Iron Nanoparticles. *Physical Review Letters* **2014**, *112*, 107201.

[16] Han, B.; Gao, X.; Lv, J.; Tang, Z. Magnetic Circular Dichroism in Nanomaterials: New Opportunity in Understanding and Modulation of Excitonic and Plasmonic Resonances. *Advanced Materials* **2020**, *32*, 1801491.

[17] Mason, R. W. *A Practical Guide to Magnetic Circular Dichroism Spectroscopy*; Wiley: New Jersey, 2007.

[18] Coey, J. M. D. *Magnetism and Magnetic Materials*; Cambridge University Press: Cambridge, 2010; Chapter 5.

[19] Reichel, V.; Kovács, A.; Kumari, M.; Bereczk-Tompa, É.; Schneck, E.; Diehle, P.; Pósfai, M.; Hirt, A. M.; Duchamp, M.; Dunin-Borkowski, R. E., et al. Single Crystalline Superstructured Stable Single Domain Magnetite Nanoparticles. *Scientific Reports* **2017**, *7*, 1–8.

[20] Kleibert, A.; Balan, A.; Yanes, R.; Derlet, P. M.; Vaz, C. A.; Timm, M.; Rodríguez, A. F.; Béché, A.; Verbeeck, J.; Dhaka, R. S., et al. Direct Observation of Enhanced Magnetism in Individual Size and Shape-Selected 3 D Transition Metal Nanoparticles. *Physical Review B* **2017**, *95*, 195404.

[21] Spaeth, P.; Adhikari, S.; Le, L.; Jollans, T.; Pud, S.; Albrecht, W.; Bauer, T.; Caldarola, M.; Kuipers, L.; Orrit, M. Circular Dichroism Measurement of Single Metal Nanoparticles Using Photothermal Imaging. *Nano Letters* **2019**, *19*, 8934–8940.

[22] Spaeth, P.; Adhikari, S.; Baaske, M. D.; Pud, S.; Ton, J.; Orrit, M. Photothermal Circular Dichroism of Single Nanoparticles Rejecting Linear Dichroism by Dual Modulation. *ACS nano* **2021**, *15*, 16277–16285.

[23] Fontijn, W. F. J.; van der Zaag, P. J.; Devillers, M. A. C.; Brabers, V. A. M.; Metselaar, R. Optical and magneto-optical polar Kerr spectra of Fe_3O_4 and Mg^{2+}- or Al^{3+}-substituted Fe_3O_4. *Phys. Rev. B* **1997**, *56*, 5432–5442.

[24] Adhikari, S.; Spaeth, P.; Kar, A.; Baaske, M. D.; Khatua, S.; Orrit, M. Photothermal Microscopy: Imaging the Optical Absorption of Single Nanoparticles and Single Molecules. *ACS Nano* **2020**, *14*, 16414–16445.

[25] Berova, N.; Nakanishi, K.; Woody, R. W. *Circular Dichroism: Principles and Applications*; Wiley: New Jersey, 2000.

[26] Oppeneer, P. M. Theory of the Magneto-Optical Kerr Effect in Ferromagnetic Compounds. Habilitation, Technische Universität Dresden, Dresden, 1999.

[27] Ge, J.; Hu, Y.; Biasini, M.; Beyermann, W. P.; Yin, Y. Superparamagnetic Magnetite Colloidal Nanocrystal Clusters. *Angewandte Chemie International Edition* **2007**, *46*, 4342–4345.

[28] Maqbool, Q.; Jung, A.; Won, S.; Cho, J.; Son, J. G.; Yeom, B. Chiral Magneto-Optical Properties of Supra-Assembled Fe3O4 Nanoparticles. *ACS Applied Materials & Interfaces* **2021**,

[29] Fan, Z.; Govorov, A. O. Chiral Nanocrystals: Plasmonic Spectra and Circular Dichroism. *Nano Netters* **2012**, *12*, 3283–3289.

[30] Chen, D.-X.; Sanchez, A.; Taboada, E.; Roig, A.; Sun, N.; Gu, H.-C. Size determination of superparamagnetic nanoparticles from magnetization curve. *Journal of Applied Physics* **2009**, *105*, 083924.

[31] Safronov, A.; Beketov, I.; Komogortsev, S.; Kurlyandskaya, G.; Medvedev, A.; Leiman, D.; Larrañaga, A.; Bhagat, S. Spherical Magnetic Nanoparticles Fabricated by Laser Target Evaporation. *AIP Advances* **2013**, *3*, 052135.

[32] Cornell, R. M.; Schwertmann, U. *The Iron Oxides: Structure, Properties, Reactions, Occurrences and Uses*; Wiley: New Jersey, 2003.

[33] Zaitoun, M.; Mason, W. R.; Lin, C. Magnetic Circular Dichroism Spectra for Colloidal Gold Nanoparticles in Xerogels at 5.5 K. *The Journal of Physical Chemistry B* **2001**, *105*, 6780–6784.

[34] Yuan, Y.; Rende, D.; Altan, C. L.; Bucak, S.; Ozisik, R.; Borca-Tasciuc, D.-A. Effect of Surface Modification on Magnetization of Iron Oxide Nanoparticle Colloids. *Langmuir* **2012**, *28*, 13051–13059.

[35] Yao, H.; Ishikawa, Y. Finite Size Effect on Magneto-Optical Responses of Chemically Modified Fe3O4 Nanoparticles Studied by MCD Spectroscopy. *The Journal of Physical Chemistry C* **2015**, *119*, 13224–13230.

[36] Ito, D.; Yao, H. Dominant Role of Iron Oxides in Magnetic Circular Dichroism of Plasmonic-Magnetic Au-$Fe_{3-x}O_4$ Heterodimer Nanostructure. *Journal of Magnetism and Magnetic Materials* **2020**, *500*, 166385.

[37] Bai, Y.; Zhang, D.; Lan, L.; Huang, Y.; Maize, K.; Shakouri, A.; Cheng, J. X. Ultrafast Chemical Imaging by Widefield Photothermal Sensing of Infrared Absorption. *Science Advances* **2019**, *5*.

[38] Li, M.; Razumtcev, A.; Yang, R.; Liu, Y.; Rong, J.; Geiger, A. C.; Blanchard, R.; Pfluegl, C.; Taylor, L. S.; Simpson, G. J. Fluorescence-Detected Mid-Infrared Photothermal Microscopy. *Journal of the American Chemical Society* **2021**, *143*, 10809–10815.

[39] Liebel, M.; Camargo, F. V. A.; Cerullo, G.; van Hulst, N. F. Widefield Phototransient Imaging for Visualizing 3D Motion of Resonant Particles in Scattering Environments. 2021; `https://arxiv.org/abs/2108.05124v1`, accessed 13 September 2021.